Understanding the ash deposition formation in Zhundong lignite combustion through dynamic CFD modelling analysis

Xin Yang [a], Derek Ingham [a], Lin Ma [a*], Hao Zhou [b], Mohamed Pourkashanian [a]

[a] Energy Engineering Group, Energy-2050, Department of Mechanical Engineering, University of Sheffield, Sheffield S10 2TN, UK

[b] Zhejiang University, Institute for Thermal Power Engineering, State Key Laboratory of Clean Energy Utilization, Hangzhou 310027, PR China

[*]Corresponding author:

Email: lin.ma@sheffield.ac.uk Phone: +44 (0) 114 21 57212.

Abstract:

A dynamic CFD model, which is based on the inertia impaction, the thermophoresis and the direct alkali vapour condensation incorporating the influence of the heat transfer to the tube, has been developed for predicting the ash deposition formation in Zhundong lignite combustion in a pilot-scale furnace. The results show that particle deposition from the inertia impaction and the thermophoresis dictates the ash deposition formation under high furnace temperatures. The deposition caused by the direct alkali vapour condensation is less significant. As deposition time increases, particle impaction efficiency decreases and sticking efficiency increases due to the thermophoresis and the local temperature conditions, which result in the time-dependent behaviour of the deposition growth. In addition, the ash deposition characteristics are influenced under different furnace temperatures, due to the change in the particle impaction and sticking behaviours. Qualitative agreement is obtained between the predicted results and the measurements for the heat flux to the tube and the ash deposition growth.

Keywords: CFD, ash deposition, Zhundong lignite, deposition mechanisms, particle behaviours.

1 Introduction

Zhundong (ZD) lignite, with a huge forecast reserve of 390 billion tons, could provide China with coal consumption for many decades [1-3]. However, due to the ZD lignite having a high content of Alkali and Alkaline Earth Metal (AAEM) elements [1-3], severe problems of ash slagging, fouling and corrosion are induced in the radiation and convection sections of the boilers [3, 4]. This can raise significant practical issues, such as reducing the efficiency and lifetime of boilers. In recent years, many efforts have been paid to experimentally study the ash deposition behaviour of Zhundong lignite combustion in lab-scale [1, 2]/pilot-scale test facilities [5-8] as well as for full scale boilers [3, 4]. The main reasons for the ash deposition problems of ZD lignite are concluded as: (i) high amount of basic components in the ZD lignite can increase the melting potential in the radiation and convection sections which cause the slagging formation [2, 5, 7, 8], and (ii) both the thermophoretic deposition of small particles and the condensation induced by the sodium related alkali vapours are responsible for the severe fouling phenomenon in the convection section of the boilers [1, 3, 8]. Although the main reasons that caused the severe ash deposition characteristics have been investigated widely, the deep understanding and prediction of the particle impaction and sticking behaviour, and the importance of the individual ash deposition mechanism on the ash deposition formation/growth is still insufficient.

CFD methods have been widely used for understanding and predicting ash deposition behaviours in combustors with different scales (lab-scale, pilot scale, and full-scale boilers) using either the 'steady state' assumptions or the dynamic simulations. Up to date, most of the publications employ the 'steady state' assumptions of the deposition rates to develop the sub-models in CFD methods (for better describing the ash deposition behaviours [9-15], for new fuels [16-20], for the oxy-combustion condition [21], etc.). This kind of assumption is suitable for the ash deposit growth on the uncooled deposition tube where the deposition surface temperature is close to the furnace temperature, which results in the stable particle impaction and sticking behaviours. In addition, the inertial impaction may be the main ash deposition mechanism under this condition [18]. However, for a real heat exchanger tube (which is cooled in boilers), the deposition surface temperature could increase with the growth of the deposit on the tube. This affects the particle impaction and sticking behaviours and the contribution of the major deposition mechanisms (inertia impaction, the thermophoretic force and the condensation) on the overall ash deposition growth. Therefore, only a dynamic consideration of the ash deposition growth is suitable for a cooled tube, rather

than a ‘steady state’ assumption. Recently, only a limited number of studies have investigated the ash deposition growth through a dynamic CFD simulation. Kaer et al. [36] developed a dynamic CFD model to predict the ash deposition formation and heat transfer rates and the paper focused on straw combustion and investigated the ash deposition rate caused by different deposition mechanisms. Wang et al. [22], Li et al. [23-25], and Balakrishnan et al. [26] developed CFD models to predict the ash deposition growth and heat transfer rate for boilers. Their models mainly considered the slag layer growth where the inertial impaction mechanisms are the main contribution. Wacławiak et al. [27, 28] modelled the ash deposit growth in the convection section based on the inertial impaction mechanism. García Pérez et al. [29] modelled the deposit growth of fume particles based on the thermophoretic force, Brownian motion and inertial impaction. In both the Wacławiak and García Pérez’s model, they focused on predicting the deposit shape and weight. The energy conservation principles were neglected in their models, which cannot consider the influence of the increase of the deposition surface temperature on the deposition behaviour. In addition, the details of particle impaction and sticking behaviours during the deposition growth process are still not clear from these previous publications [22-25, 27-31].

Therefore, this paper aims to develop a dynamic CFD model to predict the ash deposit growth process for ZD lignite combustion in a pilot-scale furnace. Understanding the initial ash deposition behaviour on cooled tubes is significant to predict the deposition propensity. Therefore, we focus on predicting the influence of the main ash deposition mechanisms, namely the inertial impaction, the thermophoretic force and the direct vapour condensation, on the deposit rate and understanding of how the deposit growth will influence the heat transfer rate through the deposit to the cooled deposition probe. In addition to the effect of furnace temperatures on the deposit growth, the particle impaction and sticking behaviours with the deposit growth are studied in-depth and the importance of the main ash deposition mechanisms on controlling the deposit growth is investigated. The model developed has been tested using the experimental data (including the deposit growth rate and the heat flux) from the Zhejiang University’s pilot-scale furnace [5].

2 Source of experimental data

Ash deposition experiments were conducted in a 300 KW pulverized fuel combustion furnace located at Zhejiang University, with an inner diameter of 0.35 m and a length of about 3.95 m. The swirl burner

consists of a primary inlet through which the pulverized coal and the primary air are fed, and a secondary inlet for the heated air to maintain a stable flame [5]. The cooled ash deposition probe, made of stainless steel, is placed in the central region of furnace, which has furnace temperatures of approximately from 1373 K to 1593 K, respectively. The probes are cooled by heat conducting oil with a temperature 503 K. In the meantime, the deposit growth is monitored online by an image sampling system. More details of the furnace and the deposition sampling system can be found in [5].

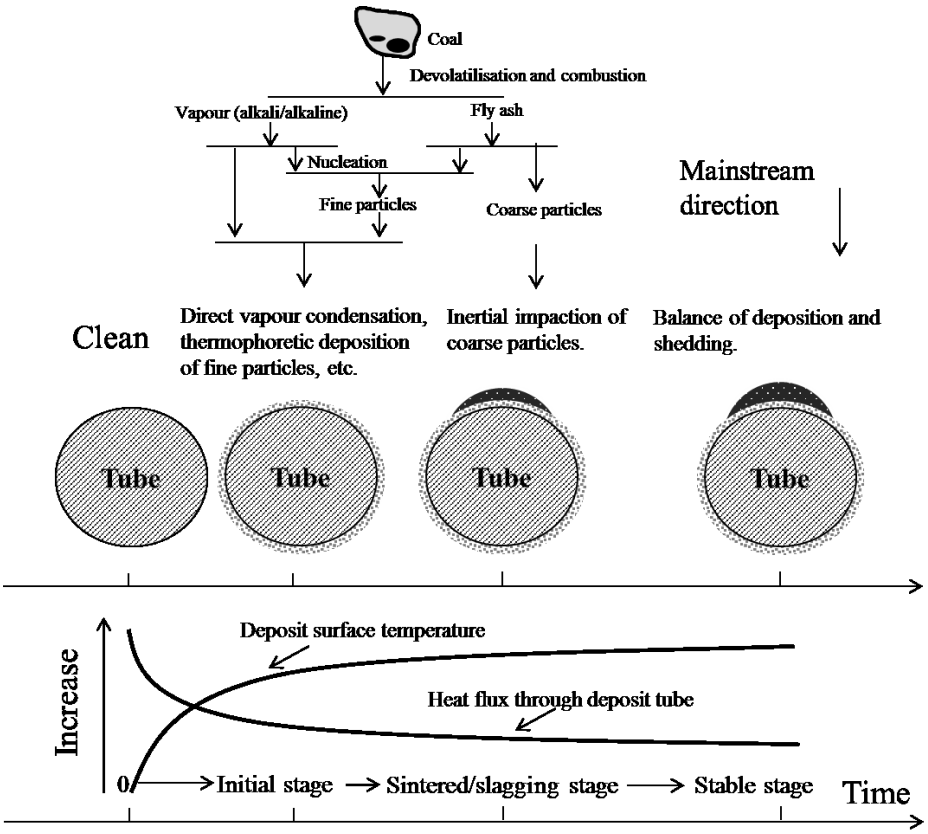

Figure 1. Schematic diagram of the main formation of the ash deposits on a cooled heat exchanger tube.

Figure 1 shows a schematic diagram of ash deposition typically formed on a cooled heat exchanger tube. Ash deposits are mainly generated by fly ash particles and the alkali/alkaline vapour after coal combustion [32]. Due to the low tube surface temperature, the deposition due to the thermophoretic force and the vapour condensation may play an important role in the ash deposit formation in the initial stage of the ash deposition formation [33-35]. The deposition surface temperature could rapidly increase due to the deposit growth and due to the rapid decrease in the heat flux to the deposition tube in the initial stage [18]. With the increase in the deposition surface temperature, the melting potential of the deposition surface is enhanced, which causes the sintering and slagging formation, the vapour condensation disappears and the contribution of the thermophoretic deposition on the arrival rate of ash particles declines [36]. At this stage,

the deposition caused by the inertial impaction of coarse particles is the main deposition mechanism. Due to the higher thermal conductivity and lower heat flux through the tube than those in the initial stage, the deposition surface temperature increases slowly and this results in the slow decrease in the heat flux through the deposition tube [18]. With the deposit growth, the shedding of the deposit is enhanced by the erosion, liquid flow at the deposit surface, gravity shedding, etc. [37]. When the shedding rate is similar to the deposition rate, the deposit growth could stop or fluctuated and then the deposit height becomes stable [38]. From the deposition test of Zhundong lignite in Zhejiang University [5], obvious shedding appears after almost two hours of deposition time. The prediction of the ash deposition behaviour is focused on the first two hours in this study, where the shedding is less important. A robust shedding model is required to capture the physics of shedding, which is considered to be a future work.

Table 1. Fuel properties of the ZD lignite [5].

Ash composition (wt.%)		*Proximate analysis (wt.%)*	
SiO_2	35.08	Volatiles (*db*)	32.79
Al_2O_3	14.04	Fixed carbon (*db*)	52.91
Fe_2O_3	6.07	Ash (*db*)	12.3
CaO	27.78	HHV(MJ/kg)	54.01
MgO	4.73	*Ultimate analysis (wt.%) (db)*	
K_2O	0.48	C	64.07
Na_2O	8.31	H	3.58
TiO_2	0.71	O	19.22
SO_2	2.8	N	0.65

Table 2. Mineral compositions of low temperature ash by XRD (*wt%*) [5].

Quartz (SiO_2)	Calcite ($CaCO_3$)	Halite (NaCl)	Hematite (Fe_2O_3)	Anhydrite ($CaSO_4$)
28.0	27.6	24.7	13.4	6.2

Table 1 shows the properties of the ZD lignite, including the proximate and ultimate analysis, as well as the major ash composition of the ZD lignite [5]. Table 2 shows the mineral compositions of the low temperature ZD lignite ash [5]. As expected, the ZD lignite has a high volatile content and low-medium ash yield. The ash analysis is dominated by silicon (Si), calcium (Ca), sodium (Na), aluminium (Al), iron (Fe) and magnesium (Mg) oxides, accounting for almost 96% of the total ash. In particular, the low

temperature ash is rich in sodium (Halite) and calcium (Calcite and Anhydrite). Additionally, quartz and hematite are present in the ash sample. The ZD lignite rich in AAEM has shown a high tendency to cause ash slagging, fouling and corrosion in the radiation and convection sections of the boilers [1-3].

3 Mathematical models

In order to describe the dynamic deposition growth of the ZD lignite, efforts have been made on producing an accurate numerical description of the ash deposition mechanisms in controlling the deposit growth and its interactions with the thermal boundary at the deposit surface. To achieve this, several submodels have been developed and applied in the CFD framework. In this section, the momentum equation to solve the particle trajectories is introduced, followed by a description on the submodels for the thermophoresis and the sticking model of the particles and the deposition surface, as well as the direct alkali vapour condensation and the deposit properties. The solving strategy of the deposition growth model with the CFD framework is discussed at the end of this section.

3.1 Particle trajectories

The arrival rate of the ash particles on the deposition surface is dictated by the particle trajectories. The particle trajectories are solved in a combined Eularian-Lagrangian frame of reference where the gas phase is modelled in the Eularian frame of reference and the ash particles are tracked in a Lagrangian frame of reference [39]. The velocity of the particles are governed by the particle momentum equation, which is a balance of the drag, gravity, and other forces as formulated in the following equation [39]:

$$\frac{d\vec{v}_p}{dt} = \frac{18\mu_g}{\rho_p d_p^2}\frac{C_D Re_p}{24}\left(\vec{v}_g - \vec{v}_p\right) + \frac{\vec{g}(\rho_p - \rho_g)}{\rho_p} + \vec{F} \quad (1)$$

where $\vec{v}$, ρ, μ and d are the velocity, density, viscosity and diameter of the particles, respectively; the subscripts p and g refer to the particle and gas, respectively, C_D is the drag coefficient, and $\vec{F}$ is the other forces, such as the thermophoretic force, the virtual mass force, the pressure gradient force, the Saffman's lift force, etc.

In this paper, both the gravitational force and the thermophoretic force are considered. The thermophoretic force, which is caused by the temperature gradient in the gas stream close to a cold deposition surface, needs to be considered when modelling the ash deposition on a cooled surface. In this paper, the thermophoretic force, $\overrightarrow{F_{th}}$, is considered by the correlations employed by Tablot et al. [39, 40]:

$$\overrightarrow{F_{th}} = -\emptyset \frac{d_p \mu_g^2}{2\rho_g T_g m_p} \nabla T \quad (2)$$

$$\emptyset = \frac{12\pi C_s (k/k_p + C_t Kn)}{(1 + 3C_m Kn)(1 + 2\,k/k_p + 2C_t Kn)} \quad (3)$$

where $\emptyset$ is the thermophoretic coefficient, T_g is the gas temperature, m_p is the particle mass, ∇T is the temperature gradient in the gas phase, $C_s = 1.17$, $C_t = 2.18$, $C_m = 1.14$, k is the fluid thermal conductivity, k_p is the particle thermal conductivity, and Kn is the Knudsen number. The virtual mass and pressure gradient forces, which are due to the acceleration of the fluid around the particle and the pressure gradient in the fluid, can be ignored when the density of the particle is much greater than the density of the fluid.

The accuracy of predicting the arrival rate of the particles is determined not only by an accurate mathematical description of the physical mechanism, but also by an accurate numerical method. Previous studies have shown that an improper grid around the deposition surface can lead to an inaccurate prediction of the particle arrival rate due to the inaccurate resolving of the flow-field within the boundary layer near the deposition surface [15, 18, 41, 42]. The accurate resolving of the flow boundary layer requires an extremely fine computational mesh close to the deposition surface. A revised particle impaction model has been developed from our previous studies [18]. It can be employed to better predict the arrival rate of the particles by resolving the particle impaction efficiency for both the drop tube furnaces and utility boilers without excessive meshing [18].

The energy balance equation for the particles, which are solved along the trajectories of the particles in order to obtain the corresponding particle temperatures, is given as follows [39, 43]:

$$m_p c_p \frac{dT_p}{dt} = hA_p(T_\infty - T_p) + \varepsilon_p A_p \sigma(\theta_R^4 - T_p^4) \quad (4)$$

where m_p, c_p, T_p, A_p, and ε_p are the mass, specific heat, temperature, surface area and emissivity of the particles, T_∞ is the gas temperature, σ is the Stefan–Boltzmann constant, and θ_R is the radiation temperature.

3.2 Sticking efficiency

In addition to the particle impaction caused by the inertia impaction and the thermophoretic force, the stickiness of the ash particles is critical to determine the fate of the particles, whether they stick on the

surface or rebounds from the surface [11, 30, 44]. Typically, the models to predict the sticking efficiency are based on such as the ash viscosity, the kinetic energy and the degree of molten of fly ash particles. The viscosity based sticking model is strongly dictated by the value of a reference viscosity. However, this value ranges within 8-10^8 Pa.s and this may contribute to an inaccurate stickiness prediction [19, 45]. The kinetic energy thresholding sticking model requires a fitting process to develop the effective Young's modulus versus the particle temperature and the particle diameter by matching the experimental data with the simulation results [13]. In addition, the ZD lignite ash has a high content of sodium and calcium, which increases the difficulty to predict the ash viscosity and the effective Young's modulus from the present modelling methodology. Further, the molten fraction-based sticking model has been developed using slag calculations based on the chemical equilibrium of the ash composition and it was found that deposition models based on the molten fraction of ash particles calculated from chemical equilibrium are promising [45]. In addition, this model is widely used for predicting the sticking efficiency of biomass ash which also contains high concentration of the alkali species [30]. Therefore, the molten fraction-based sticking model is employed to determine the sticking efficiency, η_{stick}, and it can be determined by the melt fraction of the particles and the melt fraction of the deposit on the probe surface [14, 30]:

$$\eta_{stick} = \eta_p(T_p) + (1 - \eta_p(T_p))\eta_s(T_s) \quad (5)$$

where $\eta_p(T_p)$ is the melt fraction of the particles at the particle temperature (T_p), and $\eta_s(T_s)$ is the melt fraction of the deposit on the probe at the deposition surface temperature (T_s). The melt fraction is determined by the thermodynamic equilibrium calculations based on the minimization of the Gibbs free energy from the system subject to the mass balance constraints [46, 47]. In this paper, the thermodynamic software package FactSage 7.0 is employed to perform the thermodynamic equilibrium calculations.

The calculations were performed for a temperature range between 500 K and 1750 K at a temperature interval of 20 K and at atmospheric pressure. The ash composition determined by the mineral quantity analysis of the low temperature ash and the air composition were used as the reactants. Their amounts are dictated by the inlet air/fuel ratio. It should be noticed that, in order to calculate the melt fraction of the deposit, its ash composition may be different from that of the ash particles due to the direct condensation of the alkali phases. Therefore, the local ash composition of the deposit is determined by the deposit mass of the particle deposition and the direct alkali vapour condensation calculated from the CFD results. The possible products selected are the entire compound species (ideal gases and pure solids) from the ELEM,

FToxid, FTsalt and FACTPS databases. The melt phases chosen in the calculations were the 'SLAGB' (covers liquid oxide solutions of SiO_2, Fe_2O_3, $Fe_2(SO_4)_3$ and, Na_2O, Na_2SO_4, CaO, and $CaSO_4$) and 'SALTB' (covers liquid salt solutions of NaCl, NaOH, $CaCl_2$, $Ca(OH)_2$, $FeCl_3$, $Fe(OH)_3$, etc.) with possible 2-phase immiscibility.

3.3 Deposit growth and update of deposit properties

In this paper, the deposition rate is calculated by the deposition caused by the inertia impaction, the thermophoretic force and the direct alkali vapour condensation. Therefore, the deposition rate is the summation of the deposition of these deposition mechanisms [15, 20]:

$$\frac{dR_{dep}}{dt} = A_{arrival}\eta_{stick} + I_v \tag{6}$$

where $A_{arrival}$ is the flow flux of the arrival ash particles due to the inertial impaction and thermophoretic force, η_{stick} is the sticking efficiency and I_v is the vapour condensation mass flux. Based on the assumption that the alkali phase reactions are chemical equilibrium reactions because the furnace temperature is high enough for equilibrium to be reached quickly [20]. The vapour condensation mass flux, I_v, can be determined by the following equations [20, 48]:

$$I_v = Sh(T_g)\frac{(D_v(T_g)D_v(T_s))^{1/2}}{D_h R_g}\left[\frac{p_v(T_g)}{T_g} - \frac{p_{v,s}(T_s)}{T_s}\right] \tag{7}$$

$$Sh(T_g) = 0.023Re^{0.8}Sc(T_g)^{0.4} \tag{8}$$

$$Sc(T_g) = \mu_g/(\rho_g D_v(T_g)) \tag{9}$$

where $Sh(T_g)$ is the Sherwood number, $Sc(T_g)$ is the Schmidt number, Re is the Reynold number, $D_v(T)$ is the vapour diffusivity at flue gas temperature, T_g, or deposition surface temperature, T_s, $p_v(T_g)$ is the partial pressure of the alkali vapour, $p_{v,s}(T_s)$ is the saturation vapour pressure, D_h is the hydraulic diameter of the flow channel, and R_g is the specific gas constant. In this study, only the alkali vapour of sodium chloride (NaCl) is considered since NaCl is the major alkali vapour phase of ZD lignite studied according to the chemical equilibrium calculation. For fuels with high content of potassium (K), the major K related alkali vapour phases should be considered as well.

The deposit properties (porosity, thermal conductivity, deposition surface temperature, etc.) may change with the deposit growth. Previous research indicates that these changes may have the following characteristics: (i) the deposition surface temperature can increase and the heat flux through the deposit can

decrease; (ii) the physical structure of the deposit can change from a loose and porous structure to a dense and molten structure; (iii) hence, the porosity can reduce at the sintered/slag slayer and the thermal conductivity can increase. For the initial layer, the thermal conductivity is given a value of 0.14 W/m·k [49, 50] and then the measured thermal conductivity from [5] is employed in this study, which shows the thermal conductivity will increase with the deposit growth.

A correlation based on the temperature and deposit composition is employed to calculate the deposit porosity as follows [22, 30, 31]:

$$\varepsilon_{deposit} = 1 - \left[(1-\varepsilon_0) + \frac{V_{liq}}{V_{solid}}(1-\varepsilon_0)\right] \tag{10}$$

where $\varepsilon_{deposit}$ is the deposit porosity, ε_0 is the initial deposit porosity, V_{liq} is the volume of the liquid phase, and V_{solid} is the volume of the solid phase. Calculation of the volume fraction of the liquid phase and solid phase is performed by using chemical equilibrium methods and then estimating the density of the liquid phase as a function of the chemistry using the method described by Mills et al. [51]. The deposit thickness, $L_{deposit}$, can be described as follows:

$$\frac{dL_{deposit}}{dt} = \frac{A_{arrival}\eta_{stick} + I_v}{\rho_p(1-\varepsilon_{deposit})} \tag{11}$$

The deposition surface temperature, T_{ds}, can be calculated based on the total heat flux to the probe (q_{total}) predicted from the CFD calculations, the deposit thickness ($L_{deposit}$) and the total thermal resistance (R) are as follows [23, 30]:

$$T_{ds} = q_{total}R + T_{oil} \tag{12}$$

$$R = \frac{L_{deposit}}{k_{deposit}} + \frac{L_{steel}}{k_{steel}} + \frac{1}{h_{oil}} \tag{13}$$

where T_{oil} is the temperature of the cooling oil, $k_{deposit}$ is the thermal conductivity of the deposit, L_{steel} and k_{steel} are the thickness and the thermal conductivity of the stainless steel probe, respectively, and h_{oil} is the heat transfer coefficient of the cooling oil.

3.4 Integration of the ash deposition model with the CFD framework

In this paper, the commercially available CFD software package ANSYS Fluent version 16.0 has been employed to perform the basic calculations, incorporating the in-house developed User Defined Functions and Memories in order to model the ash deposition growth process. Mathematical submodels,

such as the SST k-ω model, Discrete Ordinate model and Discrete Phase Model (DPM), were used for modelling the turbulence, radiation heat transfer and particle trajectories. In addition, the in-house developed FSCK based radiation model [52, 53] has been tested in this study, which shows similar heat transfer predictions compared to the standard WSGGM based radiation model. The present CFD model focuses on the deposition probes being placed in the central region of the furnace. A 2D geometry with a tube of diameter 40mm placed in the central region is considered as the computational domain. A fine mesh is generated around the deposition probe in order to resolve the flow-field within the boundary layer and minimize numerical inaccuracies in predicting the particle impaction efficiency. Figure 2 shows a schematic diagram of the computational domain and the meshing scheme around the deposition probe. The size of the first cell around the tube is approximately 0.3mm, which is suggested by [42, 54, 55], in order to accurately predict both the particle impaction efficiency and the particle temperature. In this paper, three cases with different furnace temperature have been investigated, namely, 1373 K, 1543 K and 1593 K. It is assumed that the discrete parcels of particles are uniformly distributed and the particles are injected through the inlet boundary condition [27-29]. The flow rate of the ash particles of 1.153 $g \cdot s^{-1}$ and the velocity of the flue gas (N_2-0.758, CO_2-0.166, O_2-0.05, H_2O-0.026, mole fraction) and particles of 2.8 $m \cdot s^{-1}$ have been used from the experiments [5]. The ash particle size ranges between 1 μm and 60 μm with a mean diameter of 16 μm and a spread parameter of 0.7 based on Rosin-Rammler distribution, which indirectly results from the original coal particle size distribution and the ash content [5, 56]. It should be noted that aerosols generated from nucleation of the alkali vapour is neglected due to the high furnace temperature [1].

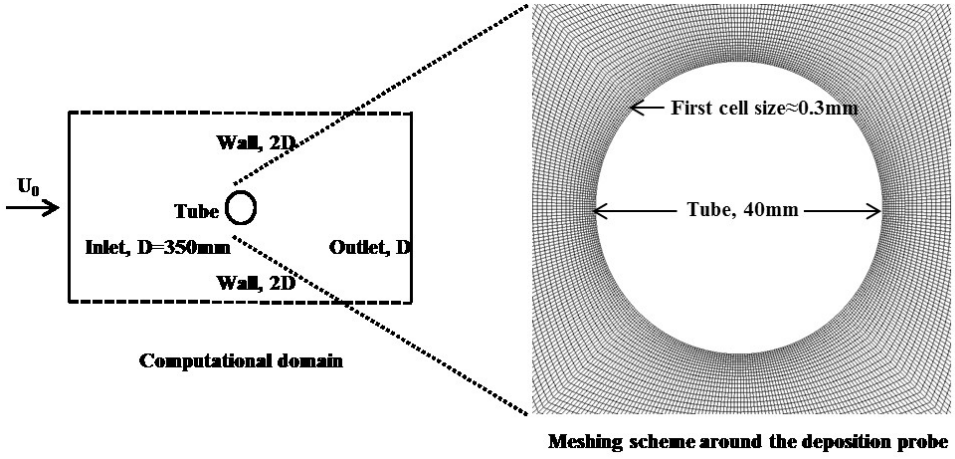

Figure 2. Schematic diagram of computational domain and meshing scheme around the deposition tube.

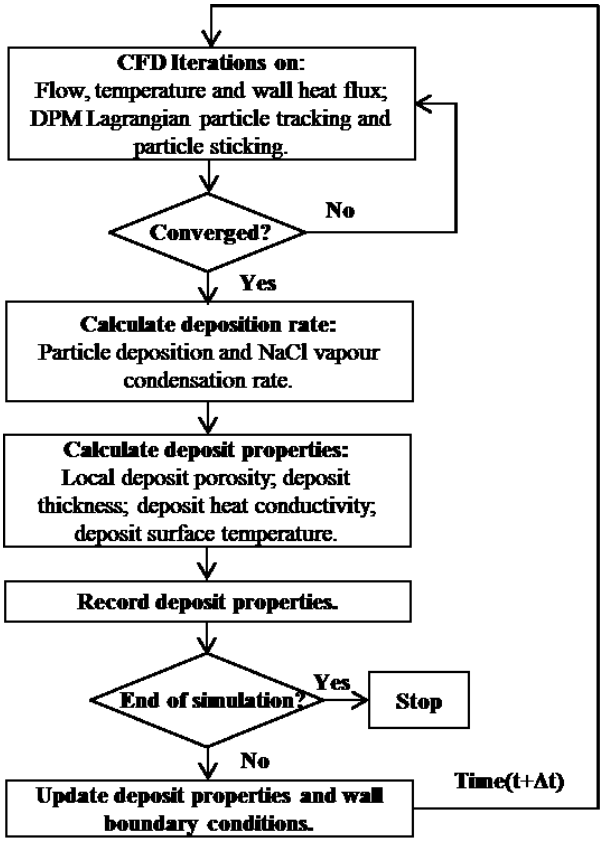

Figure 3. The algorithm of the ash deposition growth model integration in the CFD framework.

Figure 3 shows a brief flow chart of the algorithm used to carry out the simulation of the ash deposition growth process. A similar quasi-transient calculation concept has also been used to integrate the deposition model with the CFD framework [23, 26, 30]. In a time step, CFD iterations are carried out to solve the gas flow, temperature and wall heat flux. Then the Lagrangian particle tracking and particle sticking procedures are performed to determine the particle deposition. The total deposition rate can be determined by the particle deposition and the direct alkali vapour condensation rate. Then the new deposit properties (porosity, thickness, thermal conductivity, total heat resistance, etc.) are calculated, updated and stored in the User Defined Memories. In addition, a new deposition surface temperature is calculated based on the total heat flux and the total heat resistance from the updated deposit properties; the new deposition surface temperature is given to the wall boundary surface conditions by the User Defined Functions for the CFD calculation in the next time step and this process is continued until the end of the simulation. It should be noted that the simulation process starts with a clean deposition tube (deposition time=0) placed in the furnace and the initial surface temperature is predicted based on the total thermal resistance contributed from the probe itself and the cooling oil [23], as shown in Equation (12) and (13). In addition,

the calculation ends within two hours of the deposition time, where the shedding is less important [5]. The time step size is dynamically determined by limiting the increase in the deposition surface temperature in a time step to be less than 1K in order to achieve a balance between the accuracy of the simulations and the expenses of the computation time. Therefore, a time step size of 1 s was employed at the initial stage because the surface temperature increased at a high rate at this stage. The time step size gradually increased to 30s at the later stages because the increase of deposition surface temperature became very small.

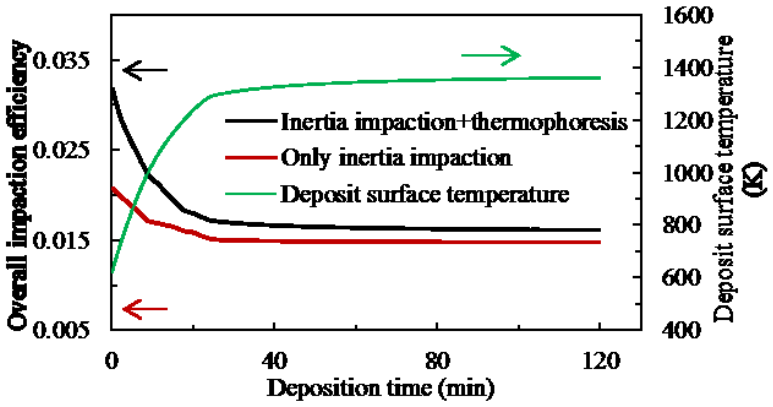

Figure 4. The overall particle impaction efficiency and deposition surface temperature as a function of the deposition time.

4 Results and discussions

4.1 Predicted results of the baseline case (furnace temperature under 1543 K)

4.1.1 Particle impaction efficiency and sticking efficiency

The prediction of the particle impaction and sticking is critical for modelling the ash deposition formation because particle impaction and sticking determine the amount of the arrival particles which may stick on the deposition probe surface. Figure 4 shows the predicted overall particle impaction efficiency (defined as the overall mass flow rate of the particles impacting on the probe to the overall mass flow rate of particles in the projected surface area) and the deposition surface temperature as a function of the deposition time. It can be found that, under the conditions without thermophoretic force and with only the inertia impaction, the overall particle impaction efficiency ($\eta_{i\_inertia}$), which has a value ranged from 0.021 to 0.015, decreases with an increase in the first 30 minutes and then it remains essentially unchanged. This is because the local condition near the deposition surface (velocity, gas viscosity, etc.) changes with

the deposition growth. Under the condition with both the inertia impaction and thermophoretic force, the overall particle impaction efficiency ($\eta_{i\_inertia+tp}$) shows a similar variance trend compared to $\eta_{i\_inertia}$. In addition, $\eta_{i\_inertia+tp}$ is larger than $\eta_{i\_inertia}$, ranging from 0.032 to 0.016. Also, Figure 5 shows that the difference of overall particle impaction efficiency between $\eta_{i\_inertia+tp}$ and $\eta_{i\_inertia}$ gradually reduces with the increase in the deposition surface temperature. This is because the influence of the thermophoretic force on the particles, which is dictated by the thermal gradient near the deposit surface, is decreased as a result of the increase in the deposition surface temperature. Therefore, the thermophorestic force contributes to the overall particle impaction efficiency by as much as 50% in the initial stage and nearly 10% at the later stage. Beckmann et al. [15] also found that the thermophoresis could increase the arrival rate of the particles by as much as 7%-50% onto the cooled deposition tube. The amount of the increased overall particle impaction efficiency (or the arrival rate) by the thermophosis is determined by the particle size distribution and the thermal gradient in the vicinity of the deposition surface.

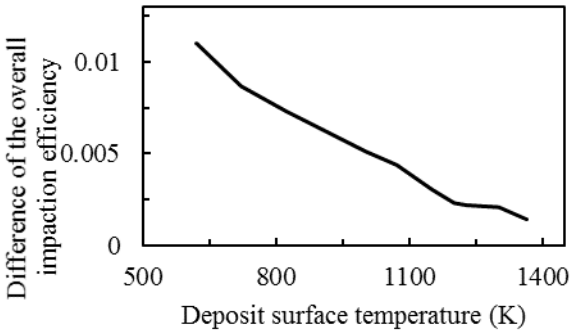

Figure 5. The difference of overall particle impaction efficiency between $\eta_{i\_inertia+tp}$ and $\eta_{i\_inertia}$ as a function of the deposition surface temperature.

In order to further investigate the influence of the thermophoresis on the individual particle impaction behaviour, the impaction efficiency of the particles as a function of the particle Stokes number is shown in Figure 6. It can be seen that, under the condition without thermophoretic force and with only the inertia impaction, the particle impaction efficiency ($\eta_{pi\_inertia}$) is very small and close to zero (smaller than 0.01) when the particle Stokes number is less than 0.1 and then the particle impaction efficiency sharply increases with an increase in Stokes number. This is because the particles with a larger Stokes number are less likely to be affected by the gas flow and more likely to impact on the deposition surface. However, particles with smaller Stokes number follow more closely to the fluid streamlines and they are less likely to impact on the surface [57]. Similar variations of the particle impaction efficiency by the inertia impaction

is also predicted in the references [18, 36, 42, 55] using the RANS, LES and DNS based CFD methods. However, under the condition with both the inertia impaction and thermophoretic force, the particle impaction efficiency ($\eta_{pi\_inertia+tp}$) is larger than $\eta_{pi\_inertia}$, as shown in Figure 6. In addition, the influence of the thermophoresis on the increase in the efficiency is enhanced with a decrease in the deposition surface temperature, as shown in Figure 6. This results in a higher increase of overall impaction efficiency with a lower deposition surface temperature as shown in Figure 4 and Figure 5.

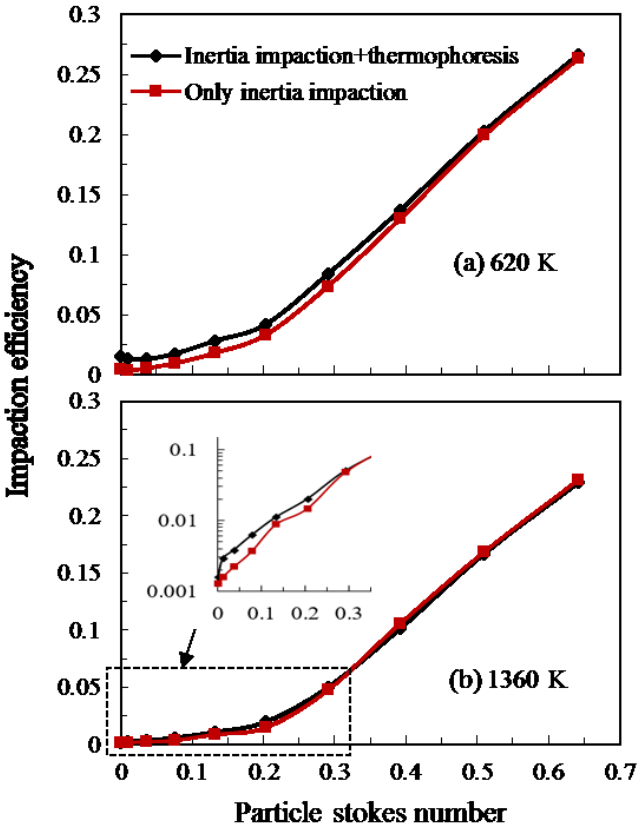

Figure 6. The particle impaction efficiency ($\eta_{pi\_inertia}$, only inertia impaction; $\eta_{pi\_inertia+tp}$, inertia impaction and thermophoresis) as a function of particle stokes number under a low deposition surface temperature (620 K) and a high deposition surface temperature (1360 K).

Figure 7 shows the predicted overall particle sticking efficiency (defined as the ratio of the overall mass flow rate of the deposited particles to the overall mass flow rate of the impacting particles) and the deposition surface temperature as a function of the deposition time. It can be observed that the overall particle sticking efficiency gradually increases with an increase in the deposition time and then it remains essentially unchanged, ranging from 0.15 to 0.58, and a corresponding increase in the deposition surface temperature, then a nearly flat variance of the temperature. It is noticed that there is a transition of a sharp

increase in the sticking efficiency and this occurs at nearly 25 mins deposition time, which corresponds to a deposition surface temperature of approximately 1230 K, as shown by the red rectangle and the red arrow in Figure 7. This is because the deposit surface starts to melt at this temperature and becomes sticky according to the chemical equilibrium calculations. It is also noted that the sticking efficiencies for the particles increase with an increase in the Stokes number. This is because the ash particles were at the cooling stage when moving towards the cold deposition surface, the small particles cool earlier and more quickly and thus have a lower temperature [13, 18].

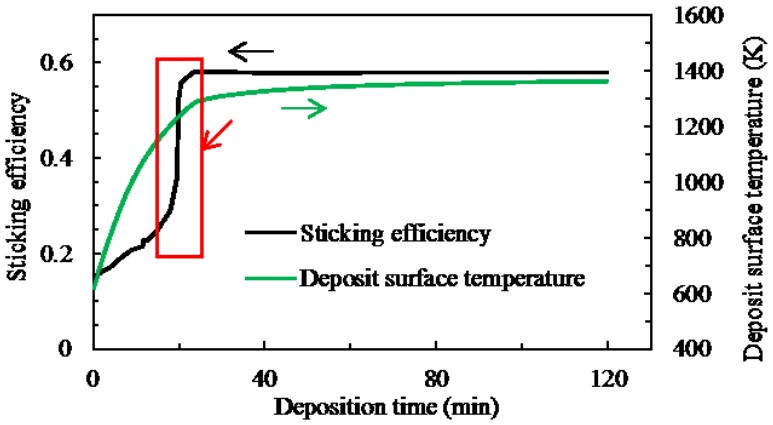

Figure 7. The overall particle sticking efficiency and deposition surface temperature as a function of the deposition time.

4.1.2 Deposition properties

In order to understand the contribution of the deposition mechanisms (the inertia impaction and the thermophoresis, and the direct vaopur condensation) on the deposition formation, the relative accumulated deposition mass (defined as the ratio of the accumulated deposition mass to the total deposition mass after two hours' deposition time) by the three deposition mechanisms as a function of the deposition time as shown in Figure 8. It is found that the relative accumulated deposition mass caused by both the inertia impaction and the thermophoresis gradually increases with an increase in the deposition time. The deposition caused by the direct alkali vapour condensation is only accumulated in the initial stage for approximately thirteen mins by the deposition model. This is because the saturation vapour pressure of the alkali phase (NaCl) increases with an increase in the deposition surface temperature. When the saturation vapour pressure is high enough, the partial pressure of the alkali vapour (NaCl) cannot support the direct vapour condensation according to the direct alkali vapour condensation model [20, 48]. In addition, it can

be seen that the relative accumulated deposition mass caused by the inertia impaction is almost eight times as large as that by thermophoresis. The relative accumulated deposition mass caused by the direct condensation is the smallest, which is hundred times smaller than that caused by the inertia impaction. In addition, the contribution of the direct condensation (defined as the ratio of the accumulated deposition mass by the direct condensation to the total accumulated deposition mass) only accounts for approximately 2% in the initial stage and 0.1% in the final stage.

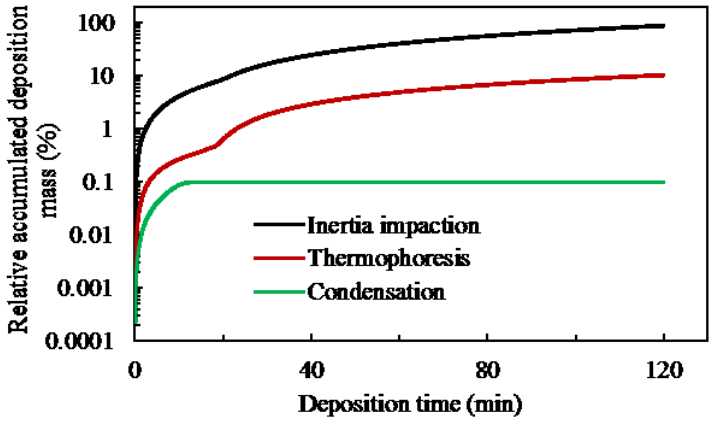

Figure 8. The relative accumulated ash deposition mass by different deposition mechanisms as a function of the deposition time.

Therefore, the predicted results suggest that the main deposition mechanisms are the inertia impaction and the thermophoresis and the contribution by the direct vapour condensation is less significant. In addition, the experimental observations of the ash composition in the different layers of the deposit show that the sodium content among all the deposit layers is less than that in the original ash and the sodium content in the inner layer is larger than that in the outer layers for the studied furnace temperature [5], which is consistent with the predicted results related to the contribution of the alkali vapour condensation. Wu et al. [8] found that the particle depositions, rather than the vapour condensation, are the main ash deposition mechanisms in the radiation section for Zhundong lignite combustion in a pilot-scale combustion test. Leppänen et al. [20] also found that the contribution of the direct alkali vapor condensation, which only contributes up to 0.01% of the total deposited mass, is insignificant. A similar direct vapour condensation model to that employed in this study [20].

However, it should be noticed that the vapour condensation may become significant for ash deposition formation in the convection section which has a much lower furnace temperature than that in the radiation

section. Under a lower furnace temperature, alkali vapour may behave under the following modes [10, 20, 58]: (i) nucleation to generate fume particles; (ii) condensation onto already existing particles; (iii) direct condensation onto the deposition surfaces. Fume particles can enhance the initial ash deposition formation on the cooled superheater surfaces by the thermophoretic force [1, 20]; the particle surfaces coated with condensed alkali phases could have a higher sticking possibility [10]. Li et al. [1] investigated the ash deposition formation of Zhundong lignite combustion in a down-fired furnace and they found that the fume particles generated by indirect alkali vapour condensation could initiate the ash deposition formation under a furnace temperature of almost 1073 K and the bulk fly ash particles with a sticky surface possibly coated by the condensed alkali vapour phases further enhance the ash deposition formation.

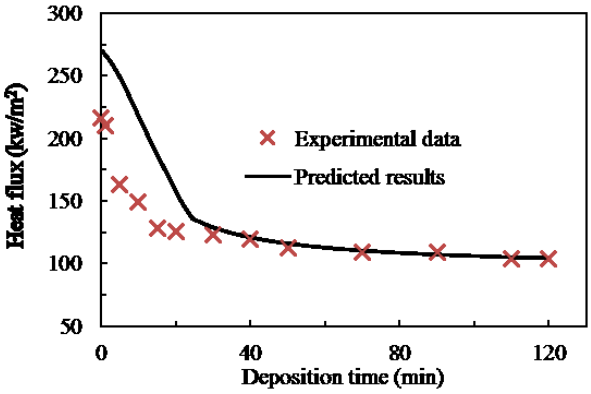

Figure 9. Comparison of the heat flux through the deposit between the predicted results and the experimental data as a function of the deposition time.

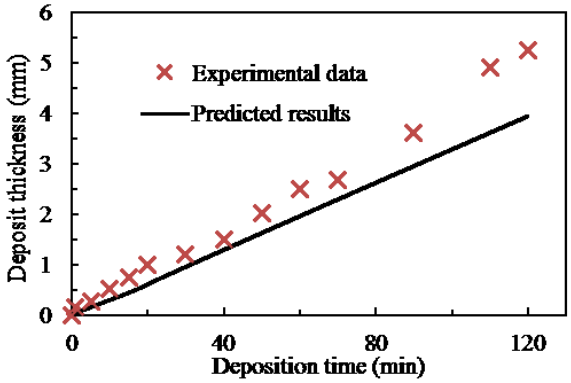

Figure 10. Comparison of the average deposit thickness between the predicted results and the experimental data as a function of the deposition time.

4.1.3 Heat transfer properties and deposition growth

In order to understand the heat transfer abatement with the ash deposition formation and growth, the heat flux (including both the predicted results and the experimental results) through the deposit as a

function of the deposition time is shown in Figure 9. Generally, it can be observed that the predictions are in reasonable agreement with the experimental data. The heat flux significantly decreases in the first half an hour and then slowly decreases in the later stages, which is consistent with the fact that the initial stage of the ash deposition is significant in the heat transfer abatement [22]. This is because the heat conductivity of the deposit is quite low in the initial stage due to its high porosity and low degree of sintering [5, 49, 50], even though the accumulated deposit at this stage is not huge compared to that in the later stage, as shown in Figure 8. The average deposit thickness (including both the predicted results and the experimental results) as a function of the deposition time is shown in Figure 10. It can be seen that the predicted deposit thickness shows a lower growth rate compared to the experimental data. This may be a result of the underestimation of the deposition rate. Up to date, it is still a challenge to quantitatively predict the particle sticking efficiency, which needs a robust sticking model to take into consideration the particle melting behaviour (ash chemistry), particle kinetic energy (particle diameter and velocity) and material properties of the particle and deposit surface, which will be considered as a future work.

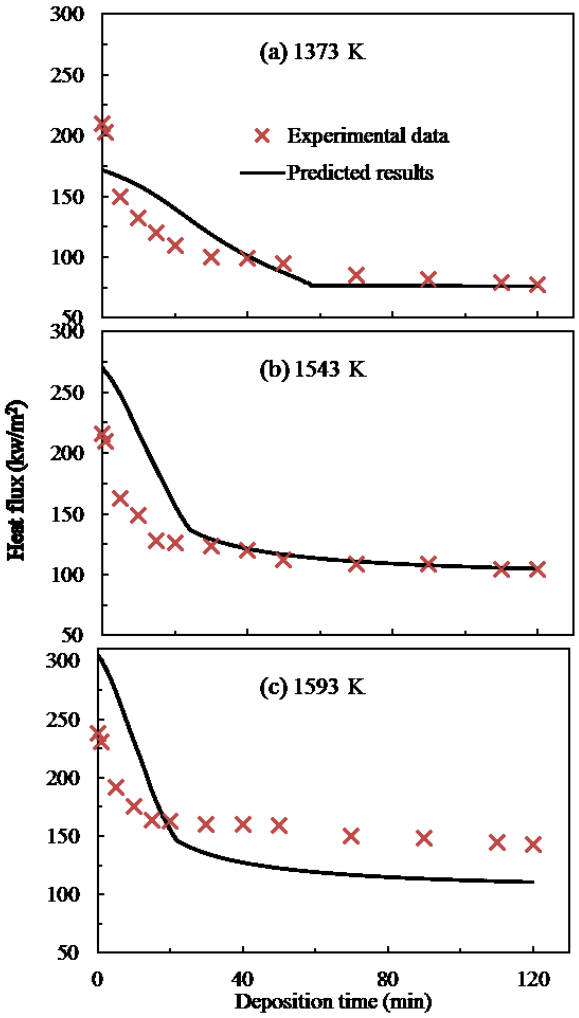

Figure 11. Comparison of the heat flux between the predicted results and the experimental data as a function of the deposition time for the three cases.

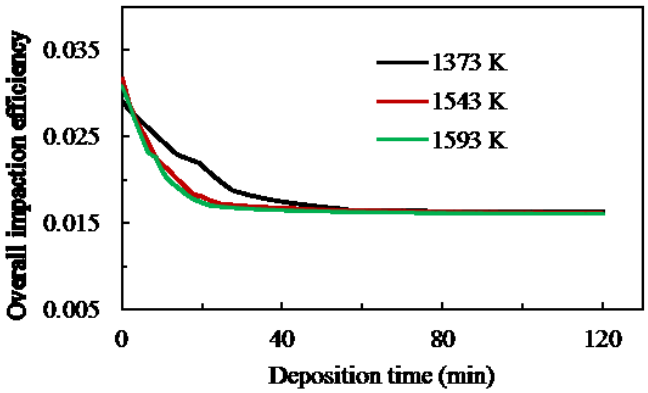

Figure 12. Overall particle impaction efficiency as a function of the deposition time under different furnace temperatures.

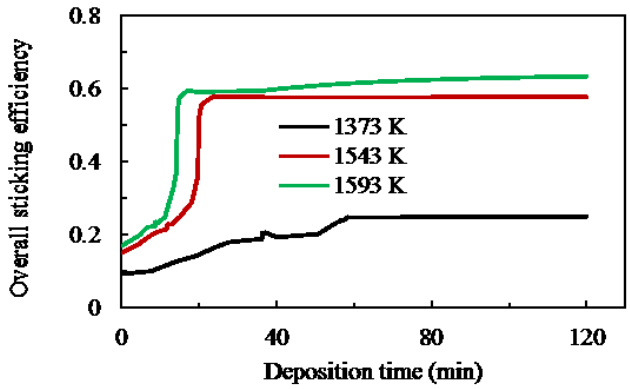

Figure 13. Overall particle sticking efficiency as a function of the deposition time under different furnace temperatures.

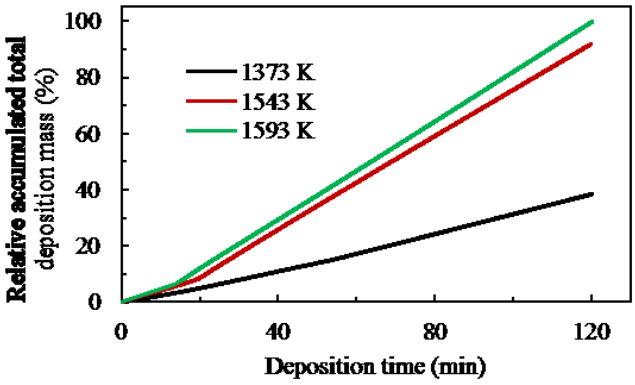

Figure 14. Accumulated total deposition mass as a function of the deposition time under different furnace temperatures.

4.2 Ash deposition formation under different furnace temperatures

The furnace temperature, which can influence the local temperature condition (the impacting particle temperature and the thermal boundary near the deposition surface), is a significant factor that controls the ash deposition formation. Therefore, it is important to investigate the ash deposition behaviour under different furnace temperatures by using the present deposition model. Figure 11 shows a comparison of the heat flux between the predicted results and the experimental data among the three different furnace temperatures as a function of the deposition time. It can be seen that the three curves show similar variance trends. Generally, it can be seen that the predictions are in reasonable agreement with the experimental data for the three cases. Also, it is noticed that higher furnace temperatures result in a higher heat flux. Figure 12 shows a comparison of the overall particle impaction efficiency for the three different furnace temperatures as a function of the deposition time. It is noticed that the 1543 K case has a similar overall impaction efficiency compared to that of the 1593 K case. At the initial stage of deposition formation, the 1373 K case has a much higher overall impaction efficiency than both the 1543 K and 1593 K cases at the same deposition time. This is because the deposition surface temperature under a lower furnace temperature is much lower than that under a higher furnace temperature at the same deposition time, which can result in a larger thermal gradient near the deposit surface and a higher thermophoresis increase in the particle impaction efficiency. Figure 13 shows a comparison of the overall particle sticking efficiency for the three different furnace temperatures as a function of the deposition time. It can be observed that the sticking efficiency increases with an increase in the furnace temperature based on the present sticking model. The efficiency reaches the highest value in the later deposition stage, 0.25, 0.58 and 0.63 for 1373 K, 1543 K and 1593 K cases, respectively. Figure 14 shows a comparison of the accumulated deposition mass (normalized by the total accumulated deposition mass after two hours' deposition time for the 1593 K case) for the three different furnace temperatures as a function of deposition time. It is found that there is much more deposit mass accumulated under a higher furnace temperature. This is mainly because there is a much higher particle sticking efficiency under a higher furnace temperature as shown in Figure 13.

Therefore, the predicted results suggest that the heat flux through the deposit increases with increasing the furnace temperature and this is confirmed by the experimental data. In addition, both the deposit mass and the deposit thickness are larger under a higher furnace temperature than those under a lower furnace temperature. This is because the particle sticking efficiency increases with an increase in the furnace

449 temperature. Wu et al. [8] also observed a higher deposition rate under a higher furnace temperature in the
450 radiation section for the Zhundong lignite combustion in a pilot-scale combustion test. However, Zhou et
451 al. [5] found that the stable deposit thickness (when the shedding rate is balanced with the deposition rate)
452 under a lower furnace temperature is higher than that under a higher furnace temperature. This may be
453 attributed to the combined effect of the deposition rate, shedding rate, and the deposit microstructure.

454 # 5 Conclusions

455 A dynamic ash deposition model based on inertia impaction, thermophoresis and direct alkali vapour
456 condensation has been developed for the modelling of the ash deposition formation on a cooled deposition
457 probe under high furnace temperatures in a pilot-scale furnace. The ash deposition model incorporates the
458 energy conversation principles to include the effect of the heat transfer on the deposition growth. In
459 addition to the growth of the deposition on the probe, the particle impaction and sticking behaviours have
460 been investigated. Also, the ash deposition behaviour under different furnace temperatures is studied
461 through the developed deposition model.

462 The predicted results for the ash deposition behaviour and the heat flux through the deposition probe
463 have been compared with the experimental data obtained from ZD lignite combustion in the pilot-scale
464 furnace and qualitative agreement is obtained. The results suggest that the ash deposition formation is
465 mainly dictated by the particle deposition from the inertia impaction and the thermophoresis under high
466 furnace temperatures. The deposition caused by the direct alkali vapour condensation is less significant.
467 The overall particle impaction efficiency decreases with the deposit growth at the initial stage and
468 stabilised at higher deposition surface temperature. This is mainly due to the decrease in the effect of
469 thermophoresis. The overall particle sticking efficiency increases with the deposit growth due to the
470 increase in the local temperature conditions (particle temperature and the deposition surface temperature).
471 The heat flux through the deposition probe significantly decreases at first and then slowly decreases as the
472 deposit builds up. Also, it is noticed that both the particle impaction and stickiness control the ash
473 deposition formation. Much higher sticking efficiency can result in a larger deposition rate under a higher
474 furnace temperature, while the calculated overall particle impaction efficiency decreases at the initial stage.
475 This is because the deposition surface temperature increases to a much higher level under higher furnace
476 temperature and this results in a lower thermophoresis influence of the particle impaction.

Acknowledgment

X. Yang would like to acknowledge the China Scholarship Council and the University of Sheffield and University of Leeds, for funding his research studies. The authors also acknowledge the support from the EPSRC grants (EP/M015351/1, Opening New Fuels for UK Generation; EP/K02115X/1, Development and Evaluation of Sustainable Technologies for Flexible Operation of Conventional Power Plants).

References

[1] Li G., Li S., Huang Q., Yao Q. Fine particulate formation and ash deposition during pulverized coal combustion of high-sodium lignite in a down-fired furnace. Fuel, 2015; 143: 430-7.
[2] Li J., Zhu M., Zhang Z., Zhang K., Shen G., Zhang D. Characterisation of ash deposits on a probe at different temperatures during combustion of a Zhundong lignite in a drop tube furnace. Fuel Process Technol, 2016; 144: 155-63.
[3] Wang X., Xu Z., Wei B., Zhang L., Tan H., Yang T., et al. The ash deposition mechanism in boilers burning Zhundong coal with high contents of sodium and calcium: A study from ash evaporating to condensing. Appl Therm Eng, 2015; 80: 150-9.
[4] Xu J., Yu D., Fan B., Zeng X., Lv W., Chen J. Characterization of ash particles from co-combustion with a zhundong coal for understanding ash deposition behavior. Energy Fuels, 2014; 28: 678-84.
[5] Zhou H., Zhou B., Li L., Zhang H. Experimental Measurement of the Effective Thermal Conductivity of Ash Deposit for High Sodium Coal (Zhun Dong Coal) in a 300 KW Test Furnace. Energy Fuels, 2013; 27: 7008-22.
[6] Zhou H., Zhou B., Zhang H., Li L. Behavior of fouling deposits formed on a probe with different surface temperatures. Energy Fuels, 2014; 28: 7701-11.
[7] Zhou H., Zhou B., Zhang H., Li L., Cen K. Investigation of Slagging Characteristics in a 300 kW Test Furnace: Effect of Deposition Surface Temperature. Ind Eng Chem Res, 2014; 53: 7233-46.
[8] Wu X., Zhang X., Yan K., Chen N., Zhang J., Xu X., et al. Ash deposition and slagging behavior of Chinese Xinjiang high-alkali coal in 3 MWth pilot-scale combustion test. Fuel, 2016; 181: 1191-202.
[9] Huang L.Y., Norman J.S., Pourkashanian M., Williams A. Prediction of ash deposition on superheater tubes from pulverized coal combustion. Fuel, 1996; 75: 271-9.
[10] Lee B.E., Fletcher C.A.J., Shin S.H., Kwon S.B. Computational study of fouling deposit due to surface-coated particles in coal-fired power utility boilers. Fuel, 2002; 81: 2001-8.
[11] Mueller C., Selenius M., Theis M., Skrifvars B.-J., Backman R., Hupa M., et al. Deposition behaviour of molten alkali-rich fly ashes—development of a submodel for CFD applications. Proc Combust Inst, 2005; 30: 2991-8.
[12] Strandström K., Mueller C., Hupa M. Development of an ash particle deposition model considering build-up and removal mechanisms. Fuel Process Technol, 2007; 88: 1053-60.
[13] Ai W., Kuhlman J.M. Simulation of coal ash particle deposition experiments. Energy Fuels, 2011; 25: 708-18.
[14] Losurdo M., Spliethoff H., Kiel J. Ash deposition modeling using a visco-elastic approach. Fuel, 2012; 102: 145-55.
[15] Beckmann A.M., Mancini M., Weber R., Seebold S., Müller M. Measurements and CFD modeling of a pulverized coal flame with emphasis on ash deposition. Fuel, 2016; 167: 168-79.
[16] Garba M.U., Ingham D.B., Ma L., Porter R.T.J., Pourkashnian M., Tan H.Z., et al. Prediction of potassium chloride sulfation and its effect on deposition in biomass-fired boilers. Energy Fuels, 2012; 26: 6501-8.
[17] Garba M.U., Ingham D.B., Ma L., Degereji M.U., Pourkashanian M., Williams A. Modelling of deposit formation and sintering for the co-combustion of coal with biomass. Fuel, 2013; 113: 863-72.
[18] Yang X., Ingham D., Ma L., Williams A., Pourkashanian M. Predicting ash deposition behaviour for co-combustion of palm kernel with coal based on CFD modelling of particle impaction and sticking. Fuel, 2016; 165: 41-9.
[19] Taha T.J., Stam A.F., Stam K., Brem G. CFD modeling of ash deposition for co-combustion of MBM with coal in a tangentially fired utility boiler. Fuel Process Technol, 2013; 114: 126-34.
[20] Leppänen A., Tran H., Taipale R., Välimäki E., Oksanen A. Numerical modeling of fine particle and deposit formation in a recovery boiler. Fuel, 2014; 129: 45-53.

[21] Brink A., Lindberg D., Hupa M., de Tejada M.E., Paneru M., Maier J., et al. A temperature-history based model for the sticking probability of impacting pulverized coal ash particles. Fuel Process Technol, 2016; 141, Part 2: 210-5.
[22] Wang H., Harb J.N. Modeling of ash deposition in large-scale combustion facilities burning pulverized coal. Prog Energy Combust Sci, 1997; 23: 267-82.
[23] Li B., Brink A., Hupa M. CFD investigation of deposition in a heat recovery boiler: Part II – deposit growth modelling. Prog Comput Fluid Dy, 2009; 9: 453-9.
[24] Li B., Brink A., Hupa M. Simplified model for determining local heat flux boundary conditions for slagging wall. Energy Fuels, 2009; 23: 3418-22.
[25] Li B., Brink A., Hupa M. CFD investigation of slagging on a super-heater tube in a kraft recovery boiler. Fuel Process Technol, 2013; 105: 149-53.
[26] Balakrishnan S., Nagarajan R., Karthick K. Mechanistic modeling, numerical simulation and validation of slag-layer growth in a coal-fired boiler. Energy, 2015; 81: 462-70.
[27] Tomeczek J., Wacławiak K. Two-dimensional modelling of deposits formation on platen superheaters in pulverized coal boilers. Fuel, 2009; 88: 1466-71.
[28] Wacławiak K., Kalisz S. A practical numerical approach for prediction of particulate fouling in PC boilers. Fuel, 2012; 97: 38-48.
[29] García Pérez M., Vakkilainen E., Hyppänen T. 2D dynamic mesh model for deposit shape prediction in boiler banks of recovery boilers with different tube spacing arrangements. Fuel, 2015; 158: 139-51.
[30] Kær S.K., Rosendahl L.A., Baxter L.L. Towards a CFD-based mechanistic deposit formation model for straw-fired boilers. Fuel, 2006; 85: 833-48.
[31] Richards G.H., Slater P.N., Harb J.N. Simulation of ash deposit growth in a pulverized coal-fired pilot scale reactor. Energy Fuels, 1993; 7: 774-81.
[32] Yang X., Ingham D., Ma L., Srinivasan N., Pourkashanian M. Ash deposition propensity of coals/blends combustion in boilers: a modeling analysis based on multi-slagging routes. Proc Combust Inst.
[33] Wang G., Pinto T., Costa M. Investigation on ash deposit formation during the co-firing of coal with agricultural residues in a large-scale laboratory furnace. Fuel, 2014; 117, Part A: 269-77.
[34] Wang Y., Tan H., Wang X., Cao R., Wei B. The condensation and thermodynamic characteristics of alkali compound vapors on wall during wheat straw combustion. Fuel, 2017; 187: 33-42.
[35] Xu M., Yu D., Yao H., Liu X., Qiao Y. Coal combustion-generated aerosols: Formation and properties. Proc Combust Inst, 2011; 33: 1681-97.
[36] U.S. Kleinhans, M. Barnerboi, S. Babat, C. Wieland, Spliethoff H. The role of thermophoresis during deposit build-up on a superheater tube[A]. In M.R. Malayeri, H. Muller-Steinhagen, A.P. Watkinson, Proceedings of international conference on heat exchanger fouling and cleaning[C], Enfield (Dublin), Ireland, 2015; 119-27.
[37] Zbogar A., Frandsen F., Jensen P.A., Glarborg P. Shedding of ash deposits. Prog Energy Combust Sci, 2009; 35: 31-56.
[38] Zhou H., Jensen P.A., Frandsen F.J. Dynamic mechanistic model of superheater deposit growth and shedding in a biomass fired grate boiler. Fuel, 2007; 86: 1519-33.
[39] Ansys, 15.0 Theory Guide, 2013.
[40] Talbot L., Cheng R.K., Schefer R.W., Willis D.R. Thermophoresis of particles in a heated boundary layer. J Fluid Mech, 1980; 101: 737-58.
[41] Weber R., Mancini M., Schaffel-Mancini N., Kupka T. On predicting the ash behaviour using Computational Fluid Dynamics. Fuel Process Technol, 2013; 105: 113-28.
[42] Weber R., Schaffel-Mancini N., Mancini M., Kupka T. Fly ash deposition modelling: Requirements for accurate predictions of particle impaction on tubes using RANS-based computational fluid dynamics. Fuel, 2013; 108: 586-96.
[43] Black S., Szuhánszki J., Pranzitelli A., Ma L., Stanger P.J., Ingham D.B., et al. Effects of firing coal and biomass under oxy-fuel conditions in a power plant boiler using CFD modelling. Fuel, 2013; 113: 780-6.
[44] Ma L., Pourkashanian M., Williams A., Jones J. A numerical model for predicting biomass particle depositions in a pf furnace[A]. In Proc ASME Turbo Expo 2006[C], Barcelona, Spain, 2006; 333-42.
[45] Wieland C., Kreutzkam B., Balan G., Spliethoff H. Evaluation, comparison and validation of deposition criteria for numerical simulation of slagging. Appl Energy, 2012; 93: 184-92.
[46] Bale C.W., Bélisle E., Chartrand P., Decterov S.A., Eriksson G., Hack K., et al. FactSage thermochemical software and databases — recent developments. Calphad, 2009; 33: 295-311.
[47] Fryda L., Sobrino C., Cieplik M., van de Kamp W.L. Study on ash deposition under oxyfuel combustion of coal/biomass blends. Fuel, 2010; 89: 1889-902.
[48] Jokiniemi J.K., Pyykönen J., Lyyränen J., Mikkanen P., Kauppinen E.I. Modelling ash deposition during the combustion of low grade fuels[A]. In L. Baxter, R. DeSollar, Applications of Advanced Technology to Ash-Related Problems in Boilers[C], Boston, MA, 1996; 591-615.

588 [49] Brink A., Laurén T., Yrjas P., Hupa M., Friesenbichler J. Development and evaluation of a long-term
589 deposit probe for on-line monitoring of deposit growth. Fuel Process Technol, 2007; 88: 1129-35.
590 [50] Robinson A.L., Buckley S.G., Baxter L.L. Experimental measurements of the thermal conductivity of ash
591 deposits: Part 1. Measurement technique. Energy Fuels, 2001; 15: 66-74.
592 [51] Mills K.C., Keene B.J. Physical properties of BOS slags. Int Mater Rev, 1987; 32: 1-120.
593 [52] Clements A.G., Black S., Szuhánszki J., Stęchły K., Pranzitelli A., Nimmo W., et al. LES and RANS of air
594 and oxy-coal combustion in a pilot-scale facility: Predictions of radiative heat transfer. Fuel, 2015; 151: 146-55.
595 [53] Clements A.G., Porter R., Pranzitelli A., Pourkashanian M. Evaluation of FSK models for radiative heat
596 transfer under oxyfuel conditions. J Quant Spectrosc Radiat Transfer, 2015; 151: 67-75.
597 [54] Bouhairie S., Chu V.H. Two-dimensional simulation of unsteady heat transfer from a circular cylinder in
598 crossflow. J Fluid Mech, 2007; 570: 177-215.
599 [55] Haugen N.E.L., Kragset S. Particle impaction on a cylinder in a crossflow as function of Stokes and
600 Reynolds numbers. J Fluid Mech, 2010; 661: 239-61.
601 [56] Backreedy R.I., Fletcher L.M., Ma L., Pourkashanian M., Williams A. Modelling pulverised coal
602 combustion using a detailed coal combustion model. Combust Sci Technol, 2006; 178: 763-87.
603 [57] Barker B., Casaday B., Shankara P., Ameri A., Bons J.P. Coal ash deposition on nozzle guide vanes—part
604 ii: Computational modeling. J Turbomach, 2012; 135: 0110151-9.
605 [58] Baxter L.L. Ash deposition during biomass and coal combustion: A mechanistic approach. Biomass
606 Bioenergy, 1993; 4: 85-102.
607